Spiraling crystallization creates layered biomorphs

Pamela Knoll, Ningjie Wu,* and Oliver Steinbock†
Florida State University, Department of Chemistry and Biochemistry, Tallahassee, Florida 32306-4390, USA

(Received 20 December 2019; revised manuscript received 19 March 2020; accepted 12 May 2020; published 9 June 2020)

Biomorphs are micrometer-sized polycrystalline structures that, despite their inorganic nature, display smoothly curved, life-like shapes. The edges of substrate-bound biomorph sheets are known to trace logarithmic spirals and can be reproduced by reaction-diffusion fronts in subexcitable media where disrupted fronts shrink tangentially. While freely rotating Archimedean spirals do not exist in subexcitable systems, our numerical simulations show that pinning sites can stabilize the rotating front. This finding is confirmed experimentally for biomorph systems that, around pH 11, produce both logarithmic and Archimedean spirals. The latter are pinned to globular $BaCO_3$ crystals and have a constant pitch in the range of 20 to 40 μm. Akin to screw dislocations, the Archimedean spirals consist of multiple layers of constant height. Their front speeds on glass and pre-existing biomorph substrate are essentially identical. We also report the detachment of intermittently pinned fronts at highly curved features of the pinning site.

DOI: 10.1103/PhysRevMaterials.4.063402

I. INTRODUCTION

Spiral shapes are a common and often striking pattern in nature with examples including the closely packed seeds in sunflowers, mollusk shells, cyclones, and spiral galaxies [1]. In materials science and crystallography, spirals occur as screw dislocations, which during growth or dissolution transform into rotating front patterns. These chiral defects have been modeled by a variety of theoretical approaches ranging from the classical Burton-Cabrera-Frank description [2] to models employing kinematic, Ginzburg-Landau, and phase field equations [3–8]. Cartwright *et al.* [9] discussed this broader type of crystal growth in terms of excitable media and emphasized specifically in the context of nacre biomineralization [10] similarities to spiral waves in chemical and biological reaction-diffusion systems, such as the CO oxidation on Pt surfaces, the autocatalytic Belousov-Zhabotinsky (BZ) reaction, and cardiac tissue [1]. These excitable systems can sustain nonlinear waves of constant speed that in head-on collisions show no interference but rather annihilate. In many cases, they also allow the formation of rotating vortices. The wave fronts of these patterns trace Archimedean spirals [11], i.e., spirals of constant pitch, and the free wave end in the spiral center describes circular (or cycloidal) trajectories.

Recently our group investigated the applicability of nonlinear reaction-diffusion models to an intriguing type of crystallization process that generates smoothly curved shapes such as leaflike sheets, helices, funnels, and coral-like structures [Fig. 1(a)] [12,13]. These typically micrometer-sized "biomorphs" are entirely inorganic and spontaneously form when an alkaline solution containing silicate ions and Ba^{2+}, Sr^{2+}, or Ca^{2+} is exposed to atmospheric CO_2 or carbonate ions [14–18]. The smoothly curved structures consist of a multitude of locally coaligned nanorods [Fig. 1(a), inset], which create a hierarchical order spanning from the nano- to the microscale and in the cases of aggregating [19] or carbonate-controlled biomorphs [20] even to length scales of several millimeters. The detailed growth mechanism of these polycrystalline aggregates is still unclear, but likely involves the formation of nanodots in solution followed by their attachment to the growth front and subsequent transformation to nanorods [21]. The latter consists predominantly of metal carbonate (e.g., witherite) with silicon-species generating detectable crystal strain [22].

Biomorph sheets are typically substrate-bound [12], about 1 μm high [23], and nucleate from metal carbonate crystallites that are often reminiscent of dumbbells measuring 5–15 μm in diameter [24]. These globules form at interfaces or in solution from which they eventually sink to the base of the container (typically glass or plexiglass). Sheets nucleate at the globule-substrate border and then expand as thin disk segments. The corresponding growth front is a curve that starts and ends at the globule. These points move along the globule border in different directions, but can detach creating a point defect that brings about a transition from an active to a stalled front. Differences in the shape of the globules and the relative time and distance of defect creation determine the shape of the resulting leaflike sheet [12].

In many cases, the edges of biomorph sheets trace logarithmic spirals that result from the local stalling of the crystallization front [Fig. 1(b)]. This propagation failure can be understood in terms of subexcitable reaction-diffusion media in which fronts with an open end shrink while continuing to move forward [Fig. 1(c)]. Notice that in an excitable system, open wave ends undergo tangential front expansion and initially straight front segments curl into rotating Archimedean spirals [Fig. 1(d)] [25]. For an initially planar wave, shrinking

*Permanent address: Nanjing Normal University, School of Mathematical Sciences, Road Qixia District, Nanjing 210046, P.R. China.
†osteinbock@fsu.edu

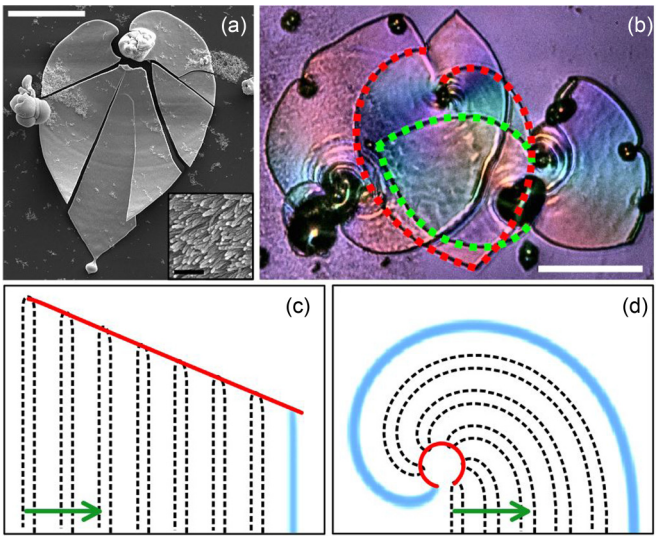

FIG. 1. (a) Scanning electron micrograph (SEM) of a biomorph sheet formed during the crystallization of $BaCO_3$ from solutions containing silicate. Inset: Nanorods on the sheet surface visualized by SEM. Scale bars: 50 μm and 200 nm (inset). (b) Optical polarization micrograph of sheets with logarithmic spirals (dashed lines) fitted to four biomorph edges. Scale bar: 50 μm. (c,d) Numerical simulation of the open end of a reaction-diffusion wave under subexcitable (c) and excitable (d) conditions. Several snapshots of the traveling waves are superposed. The red lines are the trajectories of the open wave end. Model parameter a: (c) 0.64 and (d) 0.72.

motion creates linear defect trajectories, whereas for initially circular fronts, the trajectories are logarithmic spirals. Using a simple two-variable reaction-diffusion model (the Barkley model [26] without recovery), we numerically simulated these dynamics and obtained structures that closely resemble the experimentally observed shapes [12]. Closed front curves (e.g., circles) steadily expand in both excitable and subexcitable systems.

Here we report observations of Archimedean spirals in the biomorph system. These rotating spirals are pinned to globules and-similar to screw dislocations-generate multiple sheet layers. The existence of these crystallization vortices raises the question whether pinned Archimedean spirals can exist in subexcitable systems or whether our new observation voids earlier interpretations of biomorph growth in terms of nonlinear reaction-diffusion models. We address this question by performing numerical simulations based on the full Barkley model and interpret multiple excitation events as the formation of multiple sheet layers. We find that pinned Archimedean spirals indeed occur under subexcitable conditions and characterize the minimal pinning radius that prevents detachment and defect nucleation. Our results provide additional evidence for the interpretation of the smoothly curved biomorph sheets as the result of nonlinear reaction-diffusion processes.

II. EXPERIMENTAL

Biomorphs are grown from aqueous solutions in Petri dishes (diameter 35 mm) containing small glass plates as removable sample substrates. All experiments are performed at room temperature. The initial concentrations of barium chloride and sodium silicate are 5.0 mM and 8.4 mM, respectively. The initial pH is set to a desired value by addition of a few drops of HCl solution. The Petri dishes are covered with their lids, but are not sealed. Four hours after sample preparation, we start monitoring the growth of the microstructures using an inverted optical microscope (Leica DM IRB connected to a Nikon D3300 camera) at a magnification of 40×. This optical microscopy utilizes simple bright-field illumination with or without two polarizing filters. The latter reveal the local orientation of the birefringent nanocrystals as color variations (the background color results from stress patterns in the plastic Petri dish). Image sequences are recorded at 12 frames/min. All data are analyzed using in-house MatLab scripts.

For scanning electron microscopy (SEM) and profilometric measurements, the biomorph growth is stopped abruptly by removing the glass substrates from the Petri dish. These samples are then quickly submerged in a dilute NaOH solution (pH 10). After 15 s, they are transferred to a water bath and after an additional 15 s allowed to dry under ambient conditions with two drops of acetone facilitating rapid drying. Surface heights are measured with a Dektak XT stylus profiler. For SEM, the dried samples are coated with iridium (layer thickness 6 nm) and transferred to a FEI Nova 400 field emission scanning electron microscope. Micrographs are collected at an acceleration voltage of 10 kV and a spot size of 2.5 nm.

III. MODEL AND NUMERICAL SIMULATIONS

Our simulations are based on the dimensionless Barkley model [26]

$$\frac{\partial u}{\partial t} = D_u \nabla^2 u + \epsilon^{-1} u(1-u)\left(u - \frac{v+b}{a}\right), \tag{1}$$

$$\frac{\partial v}{\partial t} = u - v, \tag{2}$$

where the system parameters ϵ, b, and D_u are kept constant at 0.02, 0.11, and 1.0, respectively, while a is varied systematically. We integrate these model equations on a two-dimensional lattice of 256×256 [280×200 in Figs. 1(c) and 1(d)] grid points using explicit Euler integration and a five-point stencil for the Laplacian. The grid spacing and the integration time step are kept constant at 0.2 and 0.008, respectively. Notice that this qualitative model aims to capture the experimentally observed dynamics but the variables and parameters are not easily matched with chemical species, concentrations, or rate constants. However, we consider u to represent the crystallization activity (possibly the associated, autocatalytic drop in pH near the growth front) and $\int v dt$ to measure the amount (i.e., height) of the solid biomorph product.

For simulations of ring-shaped annuli, two circular no-flux boundaries are generated by phase fields [27,28]:

$$\frac{\partial u}{\partial t} = \nabla \log \psi \cdot \nabla u + \nabla (D \nabla u) + \frac{1}{\epsilon} u(1-u)\left(u - \frac{v+b}{a}\right). \tag{3}$$

Before integrating Eq. (3) numerically, we first obtain the values of the phase field ψ. In practice, we set ψ to be 1 inside the ring-shaped annulus and 0 outside but integrate an auxiliary diffusion equation of the form

$$\frac{\partial \psi}{\partial t} = \xi^2 \nabla^2 \psi + (2\psi - 1) - (2\psi - 1)^3 \tag{4}$$

to smooth the interface, where the width depends on the controlling parameter ξ (here 0.05).

This phase field approach is also used for the leaf-shaped heterogeneity in Fig. 6. In the example discussed here, its specific shape is part of a hypotrochoid,

$$x = (R_h - r_h)\cos\theta + d\cos\left(\frac{R_h - r_h}{r_h}\theta\right), \tag{5}$$

$$y = (R_h - r_h)\sin\theta - d\sin\left(\frac{R_h - r_h}{r_h}\theta\right), \tag{6}$$

with $R_h = 6$, $r_h = 2$, and $d = 7$ that is rescaled to a vertical width equaling one-third of the system width.

IV. RESULTS

As the initial pH of the solution is increased from around 10 to 11, we observe an increase in the number of globules and accordingly a decrease in their average shortest distance. Under these conditions, globules do not only nucleate sheets but are also likely to act as physical obstacles to their expansion. This interaction between the moving growth front and the globules causes dynamics—to be discussed in a subsequent study—that induce multilayer growth; i.e., biomorph sheets growing on preexisting sheets. In our experiments, we have observed up to three, possibly four, layers. A typical example involving three layers is shown in Fig. 2(a), where the local number of sheet layers is indicated for a few locations. Figure 2(b) shows representative profilometric scans over three different biomorph surfaces. The sheet heights vary around the earlier reported average of about 1.1 ± 0.2 μm [23]. For each given sample, we find that the first and second layers are nearly identical in height.

Sheet-on-sheet growth also allows us to investigate potential differences between the front speeds on glass and on earlier formed biomorph surfaces. Such measurements are of interest because the mechanism controlling the biomorph thickness is not understood and could potentially involve enhanced nucleation and/or aggregation of nanoparticles on the substrate. Figure 2(c) shows superposed images of a crystallization front propagating over a pre-existing stalled front (dark nearly vertical line). The figure is generated by computing the local minimal intensity from a set of six micrographs (500 s between frames). In the case of a substrate-dependent speed, the front should show refraction and obey Snell's law [29,30]. The data in Fig. 2(c), however, show no significant deformations. To quantify this observation, we measured the growth speed of glass- and biomorph-bound sheets. Measurements were performed for initial solution pH values of 10.8–11.0 and 4–8 h after the start of the reaction. The resulting histograms [Fig. 2(d)] yield average front speeds of 0.82 ± 0.07 μm/min (on glass) and 0.81 ± 0.08 μm/min (on biomorphs). We hence conclude that the speeds, at least for these two surfaces, have a negligibly small difference or

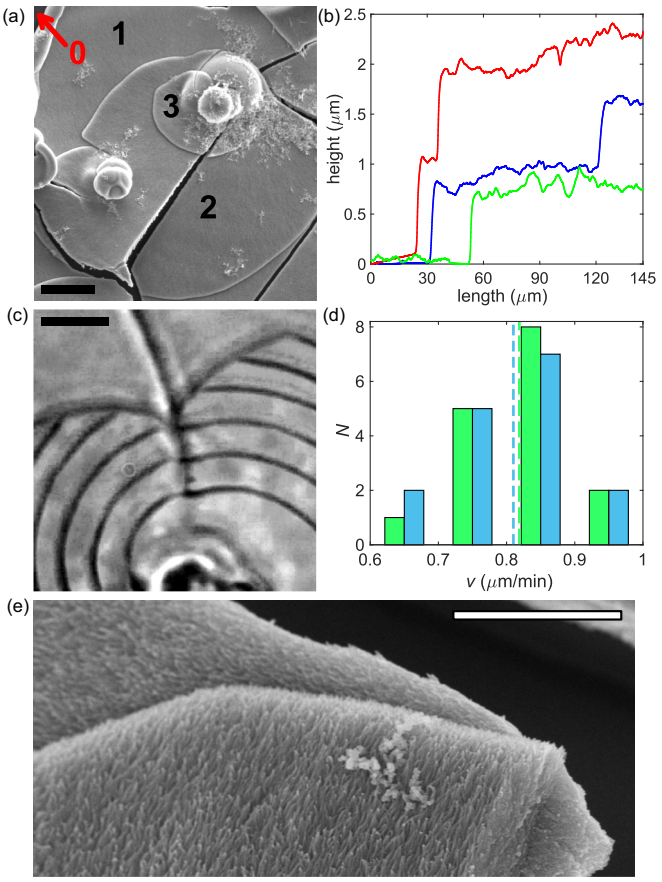

FIG. 2. (a) SEM image of a sheet structure with the local number of vertical layers indicated ("0" being the glass substrate). Scale bar: 10 μm. (b) Linear height profiles across portions of three different biomorph sheets. (c) Superposed optical micrographs illustrating the motion of a growing sheet edge (dark bands) along a stalled, inactive edge. Scale bar: 10 μm. (d) Histogram of front speeds on glass (green, left columns) and pre-existing biomorph sheets (blue, right columns). Dashed lines indicate the respective averages. (e) SEM image of a two-layer sheet resolving differently oriented nanorods. Scale bar: 2 μm.

are entirely independent of the substrate. The individual layers of the resulting biomorphs have, in general, different nanorod and crystallographic orientations that could induce interesting optical features. An example of nearly perpendicular nanotextures is shown in Fig. 2(e), where the nanorods in the upper and lower layers are coaligned in the one and four o'clock directions, respectively.

Although the speed of the biomorph fronts is the same on glass and pre-existing sheets, growing edges can be affected by sheet features in lower layers as well as other crystallization products. Figures 3(a)–3(c) show a sequence of optical micrographs recorded over the course of 29 min. Near the image center is a globule with an average diameter of 12 μm. In the upper, right image quadrant, we find a pre-existing and stationary biomorph edge (green arrow). An active front propagates nearly perpendicular to this edge and between frames (b) and (c) stalls locally, creating a cusplike feature. We observed this edge-induced stalling in numerous cases [see also Fig. 2(c)] including situations where the stalled lower

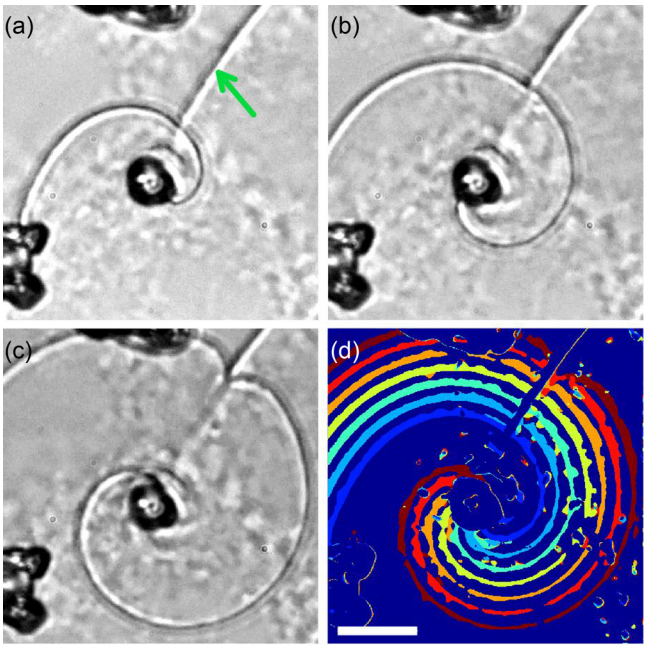

FIG. 3. [(a)–(c)] Sequence of optical micrographs of a pinned crystallization spiral. (d) Superposition of seven consecutive snapshots ($\Delta t = 250$ s) showing the same spiral. Colors indicate the local arrival time of the growth front. Scale bar: 20 μm.

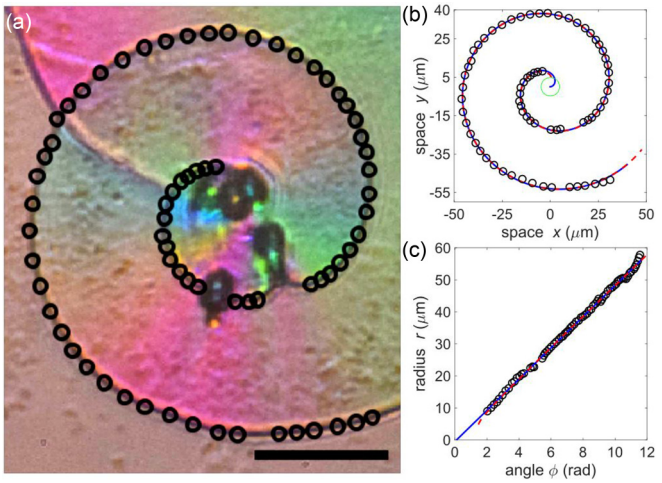

FIG. 4. (a) Micrograph of a spiral-shaped growth front. The front coordinates are measured at numerous points (open circles). Scale bar: 30 μm. (b) The blue and the dashed red curves are fits of an Archimedean spiral and a circle involute to the growth front, respectively. The circle of the involute is plotted in green. (c) The same data and fits in polar coordinates.

and stalling upper front were nearly parallel to each other. More importantly for this study, Fig. 3 shows the evolution of a pinned spiral. The rotating motion of this pattern is further illustrated in Fig. 3(d) where seven snapshots, recorded at 250-s intervals, are superposed. The different colors indicate the time of the front passage with blue and cyan being the earliest. Notice that the spiral tip is attached to the globule and traces its perimeter in the clockwise direction. The occurrence of clockwise and counterclockwise spirals appears to be equally likely.

Rotating spiral waves are a common pattern in excitable reaction-diffusion systems [1] and can either freely rotate or be pinned to unexcitable heterogeneities [31–33]. Disregarding anisotropic cases such as the CO oxidation on Pt(110) surfaces [34], their fronts are well described by the involutes of circles and Archimedean spirals. The former is the curve for which all the normals are tangent to a fixed circle, whereas the latter has a constant pitch (see Appendix). Archimedean spirals and involutes of a circle deviate only near the core. In Fig. 4, we compare the shape of pinned biomorph fronts to these mathematical curves. A representative biomorph spiral is shown in Fig. 4(a) and was obtained by optical polarization microscopy. The local color variations result from different orientations of the birefringent witherite nanorods (that are individually not resolved). From this image, we determine the front position (open markers) and replot the Cartesian [Fig. 4(b)] and polar [Fig. 4(c)] coordinates (r, ϕ). The appropriate origin is determined by minimization of the root-mean-square (rms) deviation of the experimental polar coordinates and the best linear fit.

For the experimental data in Figs. 4(b) and 4(c), we then fit an Archimedean spiral (blue line) and an involute of a circle (red dashed line). Both mathematical descriptions are in very good agreement with the experimental data and the difference between their respective rms deviations is too small to distinguish between these two very similar curves. The pitch of the Archimedean spiral is found as $\lambda = 30.6$ μm. Figure 4(b) also shows the (green) circle corresponding to the involute fit. This circle has a diameter of 9.6 μm and should approximate the boundary between the rotating crystallization front and the pinning globule. The globule in the micrograph [Fig. 4(a)] yields widths of $\Delta x = 9.0$ μm and $\Delta y = 9.2$ μm, which are comparable to the circle diameter. However, we note that the globule boundary deviates from a simple circle, which causes a slightly different involute. Despite these complications, our results clearly establish that the pinned crystallization fronts are well described by spirals of constant pitch.

In the biomorph system, pinned Archimedean spirals always exist in the presence of logarithmic spirals. The latter often demark the stalled, outer edges of a biomorph sheet, although more complicated curves are also observed. In the context of nonlinear reaction-diffusion systems, the formation of these logarithmic spirals requires subexcitable conditions for which freely rotating Archimedean spirals do not exist. Accordingly, front pinning to globules is essential for the coexistence of these two very different patterns. To investigate whether pinned Archimedean spirals exist under subexcitable conditions, we perform numerical simulations on the basis of the spatially two-dimensional Barkley model which is very similar to the FitzHugh-Nagumo model of neuronal activity. The model involves an activator variable u and control variable v. The parameters a and b define the excitation threshold $u_{\text{thres}} = (v + b)/a$ that a local perturbation in u must overcome to trigger an excitation event. Depending on the choice of parameter values, it describes excitable or subexcitable conditions with the latter occurring for small a and large b values (i.e., high values of u_{thres}). Under both conditions, the model allows for all locations to be excited multiple

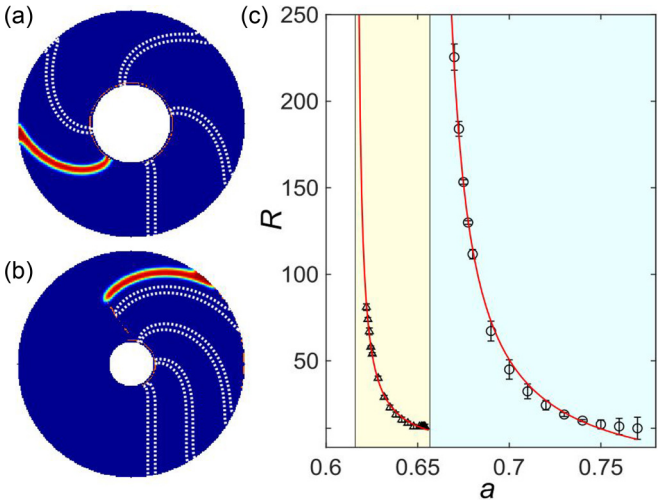

FIG. 5. Numerical simulations based on the Barkley model. [(a) and (b)] Spiral wave interacting with a disk-shaped heterogeneity under subexcitable conditions. The larger disk (a) creates a pinned vortex, whereas pinning is unsuccessful for the case of a smaller disk (b). The dotted lines show the front positions at earlier times. (c) Systematic variation of the model parameter a generates subexcitable ($0.616 < a < 0.657$) and excitable dynamics ($a > 0.657$). Open triangles denote the critical radius of the disk below which pinned state do not exist; open circles represent the core radius of freely rotating spirals.

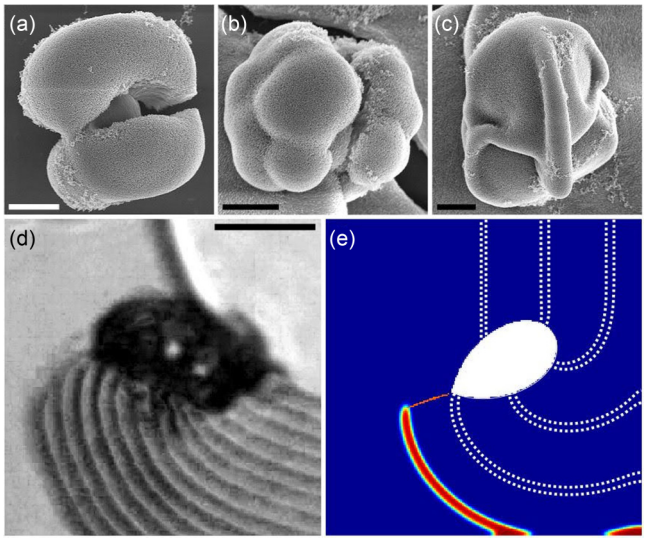

FIG. 6. [(a)–(c)] SEM images illustrating the variability in the shape of witherite globules. Scale bar: 2 μm. (d) Superposition of optical micrographs showing the detachment of the leftward moving crystallization front at a high-curvature feature of the globule (lower left corner of globule). Time between frames: 125 s. Scale bars: 10 μm. (e) Numerical simulation of an initially pinned, clockwise moving excitation front detaching at a high-curvature feature of the pinning heterogeneity (white area).

(infinitely many) times. In the biomorph system, each point can only convert once to the solid product and, hence, these multiple excitations need to be interpreted as the formation of successive sheet layers. This interpretation is justified by our finding of substrate-independent front speeds and the negligible height-to-width ratio (0.1 or smaller) of biomorph sheets. Notice that multiple excitations are impossible in the framework of Ref. [12], which used the Barkley model without recovery. In addition, we model the witherite globules as static, impermeable, and inert regions. This assumption is adequate considering the typical rotation periods of the pinned biomorph spirals (20–50 min); however, we note that the globules occasionally expand during the rotation of the spirals.

Figure 5(a) summarizes the outcome of a numerical simulation for subexcitable conditions. The active domain is ring shaped with a central hole modeling the globule. The simulation commences with an initial perturbation that triggers a linear wave segment (extending in the six o'clock direction). This wave segment begins to rotate around the globule in the counterclockwise direction and transforms into a pinned spiral wave. Figure 5(b) illustrates the outcome of a similar simulation that differs from Fig. 5(a) only by the diameter of the globule. For this smaller globule, the wave segment is pinned for only half a rotation, then detaches, and finally annihilates at the outer boundary.

The examples in Figs. 5(a) and 5(b) prove that pinned spirals exist in subexcitable media and suggest that pinning requires a sufficiently large globule. To further investigate this size dependence, we performed simulations in which the radius R of the globule was slowly decreased. These simulations reveal the existence of a critical pinning radius R_{crit} below which spirals do not pin. This pinning threshold increases with decreasing values of the model parameter a [open triangles in Fig. 5(c)]. The size of the critical radii is comparable to the system-specific core radii R_{free} of freely rotating spirals in the nearby excitable parameter space (open circles). Notice that R_{free} diverges at $a \approx 0.657$ (right vertical line), the boundary between excitable and subexcitable systems. Our results also indicate, that R_{crit} diverges to infinity but at a smaller bifurcation value ($a \approx 0.616$) below which excitation waves exist are not sustained. This divergence is further illustrated by fitting the approximating function $R(a) = A + B/(a - C)$ (red curves) to the numerical results. These fits are also used to estimate the bifurcation points between systems with no wave propagation, subexcitable dynamics, and excitable behavior (vertical lines). We also verified that the results shown in Fig. 5 are independent of the outer radius of the active medium.

The pinning sites discussed so far are circular disks, but the globules in the biomorph system often strongly deviate from this simple shape. Figures 6(a)– 6(c) show SEM images which illustrate this variability. The structure in Fig. 6(a) is close to a typical dumbbell-shaped globule, which results from the successive fractal branching of silica-poisoned barium carbonate crystals [14]. However, the globules in Figs. 6(b) and 6(c) are rather irregular, show long ridges, or are reminiscent of framboids [24,35,36], although the globules typically do not result from the aggregation of multiple crystals. The sharp corners and highly curved features of these irregular globules diminish the likelihood of crystallization fronts successfully pinning to them. Figure 6(d) illustrates this effect for a representative experiment. The figure superposes a sequence of 14 optical micrographs of a leftward moving crystallization

front (lower image half) that is initially pinned to a witherite globule (dark region in the center of the image). Once the front reaches a sharp corner of the globule, it detaches creating an open front end that departs from the globule and slowly shrinks. This phenomenon, i.e., the detachment of a transiently pinned front at a point of high curvature, can be reproduced by our simulations. Figure 6(e) shows an example in which the irregular globule is modelled as a teardrop-shaped region (white area). The front dynamics are illustrated by superposing six snapshots of a clockwise rotating front. When the front reaches the sharp tip of the anchoring site, it detaches and transforms into a shrinking front with an open end. The results of this simulation are in very good agreement with the dynamics observed in the experiment.

V. DISCUSSION AND CONCLUSIONS

In this study, we have provided additional evidence that the growth of biomorph microstructures is describable in terms of nonlinear reaction-diffusion processes. We specifically observed and characterized rotating spiral waves of constant pitch. While these familiar patterns are known to exist in systems such as the BZ reaction, Archimedean spirals had not been described in the context of biomorph growth. The subexcitable conditions of the biomorph system require that these rotating crystallization fronts are pinned to unexcitable objects. At elevated pH values around 11, such objects are readily present in the form of witherite crystals. Future studies could attempt to use lithographic techniques for the creation of cylindrical posts as pinning sites. Control over the diameter of these posts would allow the study of critical radii and the measurement of the rotation period T as a function of the pinning radius R [32]. The latter can be expected to obey $T = 2\pi R/c$, where c is the constant propagation speed of the front. In systems like the BZ reaction, curvature effects [37] and a refractory zone in the wake of the excitation pulse causes deviations from this simple dependence for small values of R. Our attempts to measure $T(R)$, or the corresponding pitch dependence $\lambda(R)$, for biomorph spirals has been unsuccessful so far, most likely due to difficulties in evaluating R for the complicated three-dimensional shapes of the pinning globules. We also note that multiarmed pinned spiral waves can exist in the BZ reaction [38] suggesting the possibility of similar patterns in the biomorph system.

The subexcitable behavior of sheet-forming biomorph solutions could be affected by system noise such as fluctuations in the concentration of the dispersed nanoparticles that extend the microstructures by attachment at the active growth edges [21]. For the example of the photosensitive BZ reaction, Kadar *et al.* showed that shrinking wave segments in subexcitable media can be stabilized by externally applied noise [39]. Such noise effects might explain unusually shaped sheet edges that we and others occasionally observe and that deviate from the reported spirals (see, e.g., Fig. 1 in Ref. [14]). Noise effects might also explain the rare disruption of fronts at locations that have no obvious heterogeneity. Unfortunately, both phenomena might also be caused by external perturbations and slow variations in certain parameters due to the acidification of the solution or fluid dynamics. Clearly more research is needed to test the relevance of stochastic processes.

Last, we restate that our study analyzes an overall three-dimensional reaction medium in terms of a two-dimensional model. Preliminary data (to be substantiated in a future study) indicate that the nucleation of pinned spirals in the biomorph system involves processes that require an explicit treatment of the vertical space coordinate. Such three-dimensional models will have to account for the self-limitation of the vertical sheet growth to about 1 μm/layer and other phenomena including the upward curling of the sheet edge.

ACKNOWLEDGMENTS

This material is based on work supported by the National Science Foundation under Grant No. 1609495 to O.S. and a Graduate Research Fellowship 1449440 to P.K. N.W. acknowledges support from the China Scholarship Council (CSC Program No. 201806865012). SEM measurements were carried out at the Condensed Matter and Materials Physics User Facility of Florida State University. We thank Professor Biwu Ma and Michael Worku for access to the profiler.

APPENDIX

Spirals are plane curves that wind around a point while moving farther away from it. Three types of spirals are relevant for this study and we have utilized their descriptions in polar coordinates (r, ϕ), specifically for comparisons with our experimental data.

(i) The Archimedean spiral is a curve described by

$$r = \frac{\lambda}{2\pi}(\phi - \phi_0), \tag{A1}$$

where λ and ϕ_0 denote the constant pitch and phase, respectively.

(ii) The involute of a circle with radius R_c is a very similar curve and given by

$$\phi = \frac{1}{R_c}\left[\sqrt{r^2 - {R_c}^2} - R_c \arccos\left(\frac{R_c}{r}\right)\right] - \phi_0. \tag{A2}$$

The range of the radial coordinate is limited to $r \geqslant R_c$. Notice that the involute of a circle can be generated by tracing the path of the end of a string as it is unwound from that circle.

(iii) The third curve relevant to our study is the self-similar logarithmic spirals [40] which is given by

$$r = a\, e^{b(\phi - \phi_0)}. \tag{A3}$$

[1] K. Tsuji and S. C. Müller, *Spirals and Vortices* (Springer Nature, Cham, Switzerland, 2019).
[2] W. K. Burton, N. Cabrera, and F. C. Frank, Phil. Trans. Roy. Soc. A **243**, 299 (1951).
[3] A. A. Chernov, J. Cryst. Growth **264**, 499 (2004).
[4] F. Falo, A. R. Bishop, P. S. Lomdahl, and B. Horovitz, Phys. Rev. B **43**, 8081 (1991).
[5] P. Smereka, Physica D **138**, 282 (2000).

[6] I. S. Aranson, A. R. Bishop, I. Daruka, and V. M. Vinokur, Phys. Rev. Lett. **80**, 1770 (1998).
[7] T. Uehara and R. F. Sekerka, J. Cryst. Growth **254**, 251 (2003).
[8] L. Gránásy, L. Rátkai, A. Szállás, B. Korbuly, G. I. Tóth, L. Környei, and T. Pusztai, Metall. Mater. Trans. A **45**, 1694 (2014).
[9] J. H. E. Cartwright, A. G. Checa, B. Escribano, and C. I. Sainz-Díaz, Phil. Trans. Roy. Soc. A **370**, 2866 (2012).
[10] J. H. E. Cartwright, A. G. Checa, B. Escribano, and C. I. Sainz-Díaz, Proc. Natl. Acad. Sci. USA **106**, 10499 (2009).
[11] A. T. Winfree, Science **175**, 634 (1972).
[12] P. Knoll, E. Nakouzi, and O. Steinbock, J. Phys. Chem. C **121**, 26133 (2017).
[13] A.-K. Malchow, A. Azhand, P. Knoll, H. Engel, and O. Steinbock, Chaos **29**, 053129 (2019).
[14] J. M. García-Ruiz, E. Melero-García, and S. T. Hyde, Science **323**, 362 (2009).
[15] P. Knoll and O. Steinbock, Isr. J. Chem. **58**, 682 (2018).
[16] M. Kellermeier, H. Cölfen, and J. M. García Ruiz, Eur. J. Inorg. Chem. **2012**, 5123 (2012).
[17] G. Zhang, C. Verdugo-Escamilla, D. Choquesillo-Lazart, and J. M. García-Ruiz, Nature Commun. **9**, 5221 (2018).
[18] W. L. Noorduin, A. Grinthal, L. Mahadevan, and J. Aizenberg, Science **340**, 832 (2013).
[19] P. Knoll and O. Steinbock, J. Phys. Chem. C **122**, 23554 (2018).
[20] E. Nakouzi, P. Knoll, and O. Steinbock, Chem. Commun. **52**, 2107 (2016).
[21] P. Knoll and O. Steinbock, Cryst. Growth Des. **19**, 4218 (2019).
[22] E. Bittarello, F. R. Massaro, and D. Aquilano, J. Cryst. Growth **312**, 402 (2010).
[23] E. Nakouzi, Y. Ghoussoub, P. Knoll, and O. Steinbock, J. Phys. Chem. C **119**, 15749 (2015).
[24] J. Eiblmeier, M. Kellermeier, D. Rengstl, J. M. García-Ruiz, and W. Kunz, CrystEngComm **15**, 43 (2013).
[25] A. S. Mikhailov and V. S. Zykov, Physica D **52**, 379 (1991).
[26] D. Barkley, Phys. Rev. Lett. **72**, 164 (1994).
[27] F. H. Fenton, E. M. Cherry, A. Karma, and W.-J. Rappel, Chaos **15**, 013502 (2005).
[28] A. Bueno-Orovio, V. M. Pérez-García, and F. H. Fenton, SIAM J. Sci. Comput. **28**, 886 (2006).
[29] J. A. Pojman, V. Viner, B. Binici, S. Lavergne, M. Winsper, D. Golovaty, and L. Gross, Chaos **17**, 033125 (2007).
[30] A. M. Zhabotinsky, M. D. Eager, and I. R. Epstein, Phys. Rev. Lett. **71**, 1526 (1993).
[31] N. Wiener and A. Rosenblueth, Arch. Inst. Cardiol. Mex. **16**, 205 (1946).
[32] O. Steinbock and S. C. Müller, Physica A **188**, 61 (1992).
[33] B. T. Ginn and O. Steinbock, Phys. Rev. Lett. **93**, 158301 (2004).
[34] P. Sadeghi, K. Dunphy, C. Punckt, and H. H. Rotermund, J. Phys. Chem. C **116**, 4686 (2012).
[35] H. Ohfuiji and D. Rickard, Earth-Sci. Rev. **71**, 147 (2005).
[36] J. Rouillard, J. M. García-Ruiz, J. Gong, and M. A. van Zuilen, Geobiol. **16**, 279 (2018).
[37] See, e.g., V. S. Zykov, Physica D **238**, 931 (2009).
[38] O. Steinbock and S. C. Müller, Int. J. Bifur. Chaos **3**, 437 (1993).
[39] S. Kádár, J. Wang, and K. Showalter, Nature **391**, 770 (1998).
[40] M. Schroeder, *Fractals, Chaos, Power Laws: Minutes from an Infinite Paradise* (W. H. Freeman & Company, New York, 1991).